Printing Patterned Fine 3D Structures by Manipulating the Three Phase Contact Line

Lei Wu, Zhichao Dong, Minxuan Kuang, Yanan Li, Fengyu Li, Lei Jiang, and Yanlin Song**

The preparation of fine 3D microstructures is an attractive issue; however, it is limited at large-area fabrication process and fineness morphology manipulation. Here, we propose a strategy to fabricate controllable 3D structures and morphologies from one single droplet via ink-jet printing. Based on the surface energy difference between the hydrophilic patterns and hydrophobic surface, the three phase contact line of a droplet contained nanoparticles is forced to pin on the patterned hydrophilic points and asymmetrically dewets on the hydrophobic surface, which leads to various morphologies. Through the regulation of pinning patterns and solution properties, the 3D morphology can be well manipulated. This strategy to control the 3D morphology of nanoparticle assembly based on hydrophilic patterns would be of great importance for fabricating controllable 3D structures.

1. Introduction

Fine 3D microstructures' fabrication has drawn great research interests in material science, such as tissue engineering,[1–3] integrated electronics,[4,5] and other advanced intelligent devices.[6,7] Current 3D fabrication methods include lithography,[8,9] materials self-assembly,[10–12] direct ink writing,[13–15] 3D printing,[16,17] etc. However, they usually suffer from complicated equipment, time-consuming processes, and insufficient controllability on precise structures. Constructing controllable 3D self-assembly microstructure in a simple and convenient way is still a challenge. Recent researches have demonstrated that nucleation, crystallization, and nanowire formation processes tend to occur along the three phase contact line (TCL) at the vapor–liquid–solid interface,[18–20] we believe that interfacial manipulation strategy is of high efficiency and manipulating TCL would present significant insights in controllable 3D manufacture. Herein, we propose a facile strategy to directly assemble nanoparticles into controllable 3D structures from one microdroplet based on 0D hydrophilic pinning pattern.

The behavior of droplet TCL, which is influenced by surface energy,[21,22] plays a crucial role on the morphology of depositions.[23,24] Specifically, for liquid droplet contained nanoparticles, TCL slides along a surface with a low surface energy in a centripetal direction, which leads to a dome-like deposition; whereas, TCL pinning typically occurs on a surface with a high surface energy, which results in a ring-like deposition.[25] In this work, we directly print 3D colloidal crystals from a single microdroplet on manually designed hydrophilic pinning patterns, as shown in **Scheme 1**. Different 3D microcolloidal crystals with precise morphologies, including line, triangle, square, star, hexagon, and octagon, are prepared by designing the 0D hydrophilic pinning patterns. In addition, through cooperative manipulation of liquid properties, such as surface tension and nanoparticle concentration, diversified 3D structures on one single pinning pattern are easily prepared. Functional materials, such as optical, electronic, and even inorganic salt, could be assembled and crystallized into precise-positioned and large-scale arrayed 3D microstructures via the use of ink-jet printing, which demonstrates the high-throughput fabrication and versatile operability. The controllable morphology of the microcolloidal crystal can be served as multi-information carriers and provide multiple optical, location and morphology information. By broadening the combination of the heterowetting substrate and the inkjet printing technology, the strategy could be anticipated to find numerous applications in biochips, information storage, and other functional devices.

2. Results and Discussions

2.1. Fabrication and Characterization of 3D Structures

Surfaces with patterned heterowettability (Figure S1, Supporting Information) were designed through introducing hydrophilic pinning points (water contact angle: 58.3° ± 1.5°) onto the homogeneous hydrophobic surface (water contact angle: 109.4° ± 1.1°). Monodispersed (<5%) poly(styrene-methyl methacrylate-acrylic acid) nanoparticles solution[26] was used to perform the 0D hydrophilic pattern induced asymmetric shrinking process. The microdroplet can be obtained through a commercial inkjet printer. **Figure 1** A,B shows the arrayed and detailed morphology

L. Wu, Z. Dong, Dr. M. Kuang, Y. Li, Dr. F. Li, Prof. L. Jiang, Prof. Y. Song
Beijing National Laboratory for Molecular Sciences (BNLMS)
Key Laboratory of Organic Solids, Key Laboratory of Green Printing, Institute of Chemistry
Chinese Academy of Sciences
Beijing 100190, P.R. China
E-mail: forrest@iccas.ac.cn; ylsong@iccas.ac.cn
L. Wu, Z. Dong, Y. Li
University of Chinese Academy of Sciences
Beijing 100049, P.R. China

DOI: 10.1002/adfm.201404559

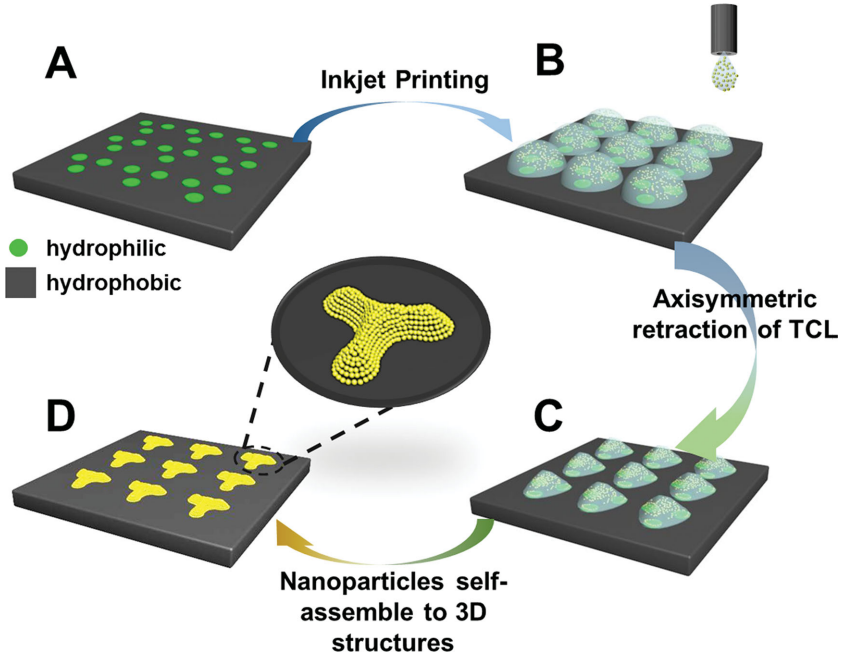

Scheme 1. Manipulating 3D morphology of microcolloidal crystal pattern through hydrophilic pattern induced asymmetric dewetting. A) A hydrophobic silicon wafer with patterned hydrophilic pinning spots (green shading) was used as substrate. B) Through ink-jet printing, nanoparticles contained droplets array was prepared with designed location. C) Triangle shaped droplets array was formed by hydrophilic pattern induced asymmetric dewetting. D) Arrayed 3D microcolloidal crystals with controllable morphology were achieved.

of typical triangle shaped microcolloidal crystal, which was controlled by three separated hydrophilic pinning points. Such morphology proves that nanoparticles move along with the asymmetrically shrinking TCL and the nanoparticle assembly replicates the morphology of the droplet during dewetting process, such that well-defined microcolloidal crystals with controllable morphology can be achieved. Generally, nanoparticles pack tightly on a hydrophobic surface, on which the droplet has a large surface receding contact angle (θ_R), while pack loosely on a hydrophilic surface with a small θ_R.[27] Closely packed morphologies are assumed to have superior properties for practical applications and numerous efforts have been made to achieve a uniform deposition by adjusting particle shapes and regulating capillary flow.[28,29] Here, through manipulating the retracting TCL by 0D hydrophilic pattern, the assembly of nanoparticles on the hydrophobic region with large θ_R as well as on the hydrophilic region with small θ_R presents a hexagonal closely packed structure (Figure 1D,E). Theoretically, as TCL is pinned on the hydrophilic region, capillary flow from the hydrophobic to the hydrophilic regions offers a driving force to carry and push the nanoparticles to the hydrophilic regions.[30] Whereas with the confinement of the liquid module (Figure 1C), a uniform triangle microcolloidal crystal is finally prepared, which can functionally lead to bright structural color and is potential of being used as functional unit.

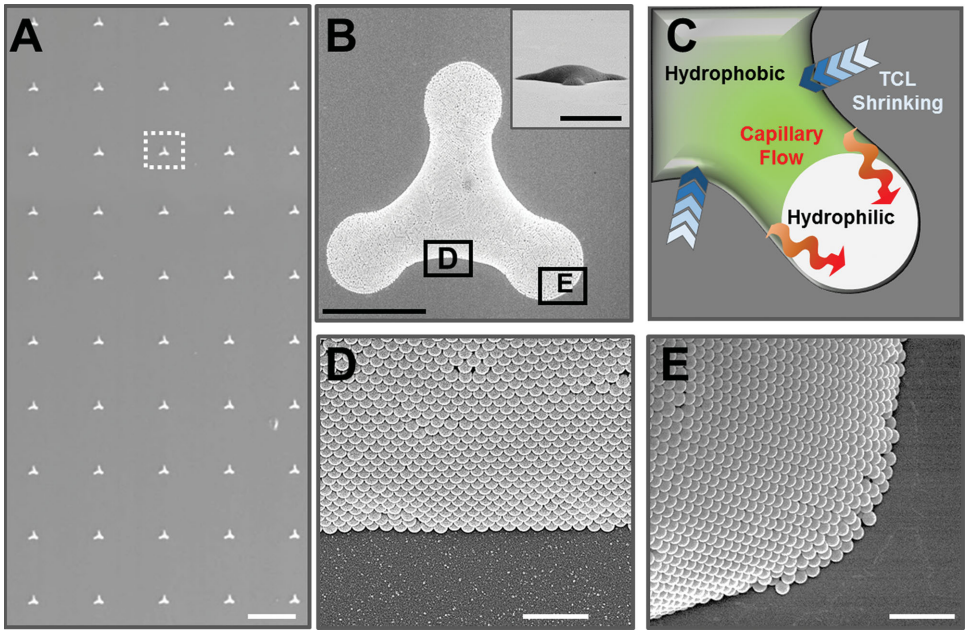

Figure 1. Typical morphology of the 3D microcolloidal crystals induced by hydrophilic pinning pattern. A) Scanning electron microscopy (SEM) image of arrayed microcolloidal crystals in a large-scale. B) Top-view SEM image of a compactly assembled microcolloidal crystal structure. Inset: Side-view SEM image of the microcolloidal crystal. C) Mechanism scheme of nanoparticle assembly on the hydrophilic region. D) and E) are enlarged SEM images of the hydrophobic and hydrophilic regions, which represent the corresponding locations in B), respectively. The assembly of nanoparticles displays high quality colloidal crystal structures both on the hydrophobic and hydrophilic regions. Scale bar: 200 μm A) and 20 μm B). Scale bar: 10 μm D,E).

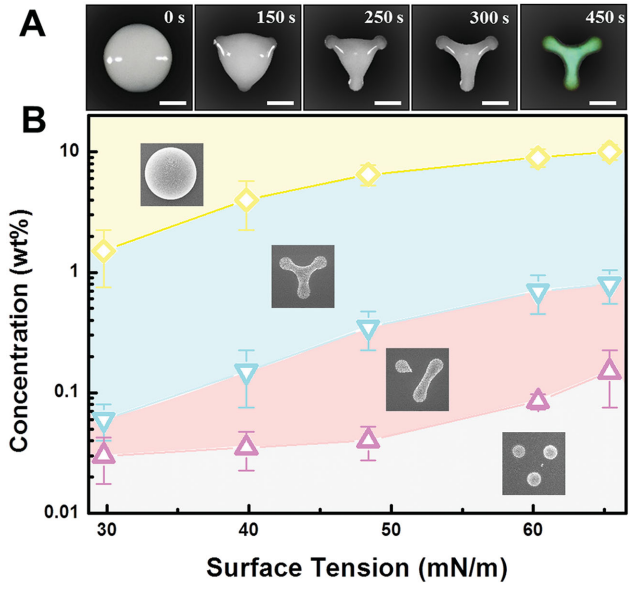

Figure 2. The formation mechanism and the process of a single microcolloidal crystal on the pinning points patterned hydrophobic substrate. A) Optical images of the asymmetric dewetting process for the formation of designed 3D structure. B) The influence of the surface tension and concentration on the morphology of the microcolloidal crystals. Insets are representative SEM images of corresponding morphologies. Scale bar: 10 μm A).

2.2. Dynamic Formation of 3D Structures

The dynamic formation process for a triangle shaped microcolloidal crystal was monitored in real time, and corresponding images of different dewetting states were illustrated in **Figure 2**A. With solvent evaporation proceeding, TCL first retracted uniformly inward on the hydrophobic region. Whereas, the pinning hydrophilic points with high surface energy served as dewetting defects to confine this shrinking process subsequently. As a result, TCL pinned on the periphery of the three hydrophilic points for substrates with triangle spaced pinning points. With further retracting of TCL on the hydrophobic surface, asymmetric shrinking of TCL occurred (pinning on the hydrophilic points and sliding on the hydrophobic region along the periphery of the patterned hydrophilic points), which leads to the formation of triangle shaped liquid membrane with controllable 3D morphology. Simultaneously, nanoparticles followed the motion of TCL and assembled along the curved surface of the droplet, which finally formed triangle 3D structures (Figure S2, Supporting Information). These photonic crystal microstructures exhibit a bright reflected green color due to the Bragg scattering from the periodic lattice.[31] Accordingly, closely packed 3D assembly of microcolloidal crystals can be prepared through this hydrophilic pattern manipulating TCL method.

Figure 2B shows the overall relationship between the droplet properties and the final 3D morphologies of microcolloidal crystals. Insufficient surface tension or concentration of a liquid could result in a 3D morphology with discontinuous scattering fragments with one neck or two necks ruptured (Figure 2B, grey and pink shading); whereas, in the yellow shading of Figure 2B, high concentration or surface tension of a droplet results in excess nanoparticles spilling over a single pinning pattern unit. An appropriate concentration (ranging between the minimum concentration C_{min} and the maximum concentration C_{max}, which are blue line and yellow line of Figure 2B, respectively) and a proper surface tension are thus needed for the successful formation of the microassembly.

2.3. Formation Mechanism of 3D Structures

Having clarified the suitable concentration and surface tension of solution for successful preparation of microcolloidal crystals, force analyses concerning the distorted TCL are then investigated to interpret the mechanism of TCL asymmetric dewetting and to predict the final 3D morphology. The morphology of the microcolloidal crystal is dominated by three competitive forces: one driving force and two resistance forces (**Figure 3**A). The driving force $F_{\Delta RCA}$ is typically generated by surface energy difference, which acts as a motivation for TCL asymmetric retraction. Due to the variation of surface chemical composition, surface energy difference generates and the difference of which will lead to varying receding contact angles (θ_R). Such θ_R difference will induce the asymmetric dewetting of TCL, as shown in Figure 3A, which results in the distortion of TCL. The distorted TCL further causes the deformation of the droplet from hemidome to different controllable morphologies corresponding to the pattern of hydrophilic pinning points (Figure S3, Supporting Information). The driving force of asymmetrically moving TCL which arises from θ_R difference is given by[32]

$$F_{\Delta RCA} = \Delta l_1 \gamma \cos\theta_{R1} - \Delta l_2 \gamma \cos\theta_{R2} \quad (1)$$

where γ is the surface tension of the dispersion, θ_{R1} and θ_{R2} are the receding contact angles of dispersion on thehydrophilic and hydrophobic region, respectively. Δl_1 and Δl_2 are effective length of different wettabilities.

The resistance forces which operate to counteract $F_{\Delta RCA}$ are mainly ΔP ascribed from the TCL asymmetric retraction and F_{PS} generated from adhesive force between nanoparticles and substrate nearby TCL,[33–35] which can be expressed as

$$F_{resistance} = A\Delta P + F_{PS} = A\int_{w_1}^{w_2} \gamma\left(\frac{1}{r}+\frac{1}{R}\right) dw + 6\pi R_{PS}\sqrt{\frac{G^*}{E^*}\Delta\gamma} \quad (2)$$

where A is the contact area on the substrate, w is the width of the liquid film, w_1 and w_2 are the stopping and starting position of TCL, respectively. r and R are the local radiuses which are influenced by w. R_{PS} is the radius of nanoparticle; G^*, E^*, or $\Delta\gamma$ is the average shear modulus, average Young's modulus, or average surface energy of particle and substrate, respectively (Scheme S1, Supporting Information).

2.4. Morphology Manipulation of 3D Structures

The final morphology of the microcolloidal crystal can be deduced by balancing the relative acting ingredients as $F_{\Delta RCA}$ equals $F_{resistance}$, which are related with liquid properties, such as surface tension and nanoparticle concentration, and the 0D pinning pattern parameters, such as pinning points' geometrical

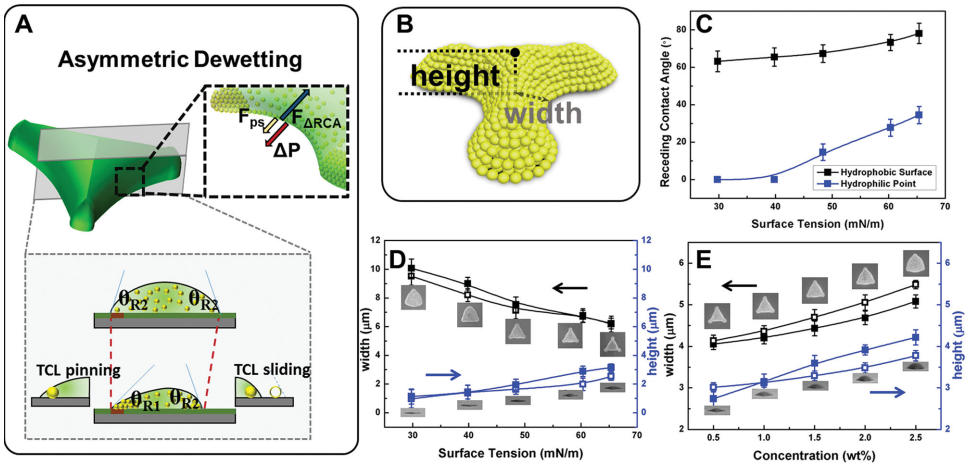

Figure 3. Tunable 3D morphology of microcolloidal crystals via asymmetric dewetting. A) Mechanism of pinning points induced asymmetric dewetting and assembly. The surface energy difference leads to θ_R difference which drives asymmetric dewetting of TCL. B) Schematic morphology and geometrical parameters of the 3D structure. C) θ_R influenced by the variation of surface tension on the hydrophilic (blue) and hydrophobic (black) region, respectively. D) Width (black), height (blue) versus nanoparticle concentration with a fixed surface tension. Solid points represent experimental results and hollow points indicate theoretical results. E) Adjusting the structures of the 3D microcolloidal crystals through manipulating the surface tensions with a fixed concentration: black and blue points are width and height, solid and hollow points are theoretical and experimental results, respectively.

shape, distance, arrangement, and wetting property. In order to visually elaborate the 3D structure, we define width and height of the microcolloidal crystal to represent its horizontal and longitudinal dimension (Figure 3B). The liquid property influenced 3D morphology is first investigated. Theoretically, the variation of surface tension affects corresponding θ_R, which further influences the retracting ability of TCL as well as the 3D morphology of the microcolloidal crystal. For dispersion with a fixed concentration, θ_{R1} and θ_{R2} increased with the increasing of the liquid surface tension (Figure 3C). Thus, the droplet with a higher surface tension possesses a relatively larger driving force $F_{\Delta RCA}$, which can be calculated from Equation (1). The larger driving force will lead to a larger retracting distance and a more stereoscopic morphology (Figures S4 and S5, Supporting Information). On the contrary, a flatter microassembly would be formed for dispersion with a low surface tension on the surface. By balancing Equations (1) and (2), the width decreases and the height increases with the increasing of surface tension, which is consistent well with the experimental results in Figure 3D. Adjusting solute composition without changing liquid surface tension, the 3D morphologies remained similar (Figure S6, Supporting Information). As a result, with the regulation of liquid surface tension, tuneable 3D morphologies could be prepared on the same pinning pattern, demonstrating the morphology diversification of this method.

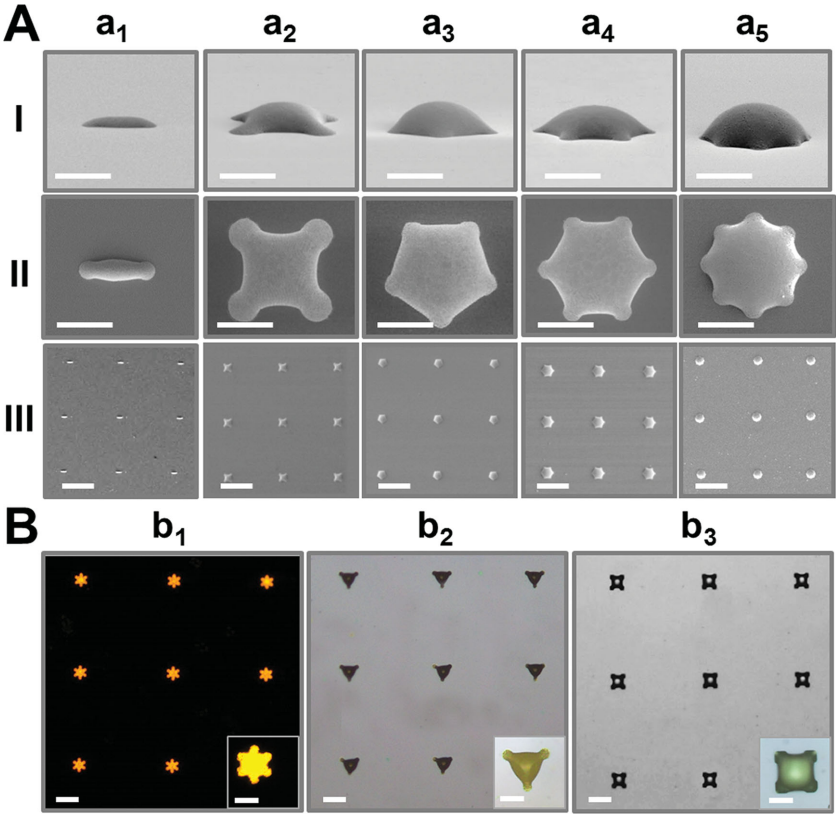

Figure 4. Morphology manipulation of various assembly units through designed hydrophilic pinning pattern. A) Controllable 3D structures include line a_1), quadrilateral a_2), star a_3), hexagonal a_4), and octagon a_5) were prepared. I), II), and III) are side-view, top-view, and arrayed SEM images of corresponding morphologies, respectively. B) The morphology of microassemblies composed of various materials: CdTe quantum dots b_1), silver nanoparticles b_2), and manganese chloride salt (b_3) could be manipulated. Insets are enlarged images of corresponding microassembly, respectively. Scale bar: 20, 20, and 100 μm (a_I, a_{II}, and a_{III}), respectively. Scale bar: 50 μm B) and 20 μm in the inset of B).

For dispersion with fixed surface tension, the 3D morphology can be manipulated via regulating the particle concentration, which dominates F_{PS} when nanoparticle concentration ranges between C_{min} and C_{max}. Experimentally, the increase of nanoparticle concentration mainly influences F_{PS} (Figure S7, Supporting Information), while has slight influence on the liquid surface tension (Figure S8, Supporting Information). By balancing the competitive forces, the theoretical width and height can be calculated, which fits well with the experimental data plotted in Figure 3E. The slight flatter curve of width than height can be attributed to the delicate influence of nanoparticle concentration on the liquid surface tension and θ_R, which decreases the retracting ability of TCL (Figure S9, Supporting Information). In addition, the width and height of the 3D structures will reach their maximum thresholds when concentration or surface tension of the droplets are so high that lead to excess nanoparticles spilling over a single pinning pattern unit (Figure 2B, yellow shading).

Besides liquid properties, the diversified 3D morphology can also be regulated through the variation of pinning pattern parameters. Increasing surface energy difference of the heterowettable substrate, a more stereoscopic morphology can be achieved (Figure S10, Supporting Information). Whereas regulating the distances between hydrophilic pinning points, the size of the microcolloidal crystal can be further manipulated as shown in Figure S11, Supporting Information. In addition to the triangle confined morphology, quadrilateral, hexagon, or even arbitrary 3D structures have been acquired (**Figures** 4A and S12, Supporting Information). Other microcolloidal crystals can be obtained by designing the pinning point pattern and geometry (Figures S13–S15, Supporting Information). Furthermore, 3D microcrystalloids of metal (silver) nanoparticles, quantum dots (CdTe) and even inorganic salt (manganese chloride) were fabricated (Figure 4B), demonstrating that this general strategy can construct 3D structures with various materials.

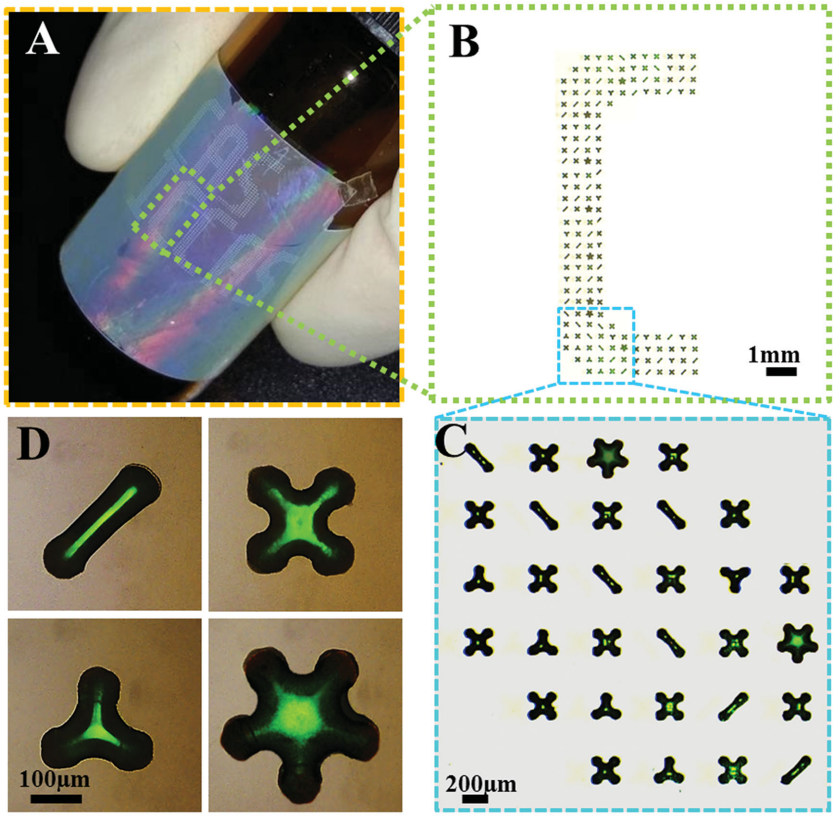

Figure 5. The microcolloidal crystals with controllable 3D morphology used as a multi-information carrier. A) "ICCAS" (Institute of Chemistry, Chinese Academy of Sciences) in which single unit is composed of pinning pattern induced microcolloidal crystals. B) Enlarged optical image of the single letter "C." C) Enlarged optical image of part of "C." D) Detailed optical images of single information carrier dot with bright structural color. Scale bar: 2 mm B), 500 μm C), and 100 μm D).

2.5. Application of the 3D Structures as Information Carriers

Encouraged by the controllable morphologies and photonic properties of the 3D microcolloidal crystals, we design a macro/microhierarchical structure color pattern (**Figure 5**A), which is of great significance for the fabrication of multi-information carrier or anticounterfeiting materials. As shown in Figure 5B–D, the printed 3D array displays bright structure color even with the existence of reflective rainbow color. The composition, morphology, and location of each single 3D structure as well as their permutation and combination could be well manipulated, which is of potential being used as multiprotocol optical codes (Figures S16 and S17, Supporting Information).[36] As well-defined 3D architectures can lead to collective functional properties,[37,38] the as-prepared hierarchical pattern will be promising for development of novel photonic and other functional devices.

3. Conclusions

In summary, we have demonstrated a new approach to fabricate controllable 3D microstructures from a droplet on a hydrophilic pinning points patterned substrate via ink-jet printing. The asymmetric dewetting of the droplet's TCL leads to the assembly of nanoparticles into various 3D morphologies with closely packed structures. Through the cooperative regulation of liquid properties and the pinning points' parameters, the 3D morphology can be precisely designed and well controlled. The 3D structures can serve as multi-information carriers through regulating the composition, morphology, and location of each single 3D structure as well as their permutation and combination. Developing other functional materials as inks, such as quantum dots and metal nanoparticles, 3D microstructures with desired morphologies can be achieved, providing this approach a promising future in 3D manufacture.

4. Experimental Section

Materials: Monodispersed (<5%) poly(styrene-methyl methacrylate-acrylic acid) nanoparticles with a mean diameter of 210 nm were obtained from our laboratory using previous synthesis method.[27] Silver nanoparticles were purchased from Suzhou Coldstones Tech. Co. Ltd., CdTe nanoparticles were purchased from ZhongKeWuYuan Biotechnology Co. Ltd. Manganese chloride and ethylene glycol were purchased from J&K chemical Co. Ltd. 1H,1H,2H,2H-perfluorodecyltrimethoxysilane (PFOS) and octyltrichlorosilane were purchased from Sigma-Aldrich. ⟨100⟩-oriented silicon wafer was purchased from Institute of Semiconductors, Tianjin, China.

Ink and Substrate Preparation: Printing inks with different surface tension were prepared by adding ethylene glycol or ethanol into nanoparticle-water dispersion. The concentration of dispersion used in the experiment ranges between 0.5 and 5.0 wt%. Before printing, the ink was treated ultrasonically and filtrated through a nylon mesh with diameter of 1.0 μm. The substrate with heterowettability was prepared through photolithography and then postgrafted with PFOS. After removing the photoresist, the preprotected region shows hydrophilicity which acts as the hydrophilic pinning pattern, while the unprotected region shows hydrophobicity.

Printing Conditions: The latex inks were printed by a Fujifilm Dimatix DMP 2800 printer with 10 pL cartridges and printing orifice with the diameter of 25 μm. The ink was ink-jet printed onto substrate and then allowed to dry at 25 °C and relative humidity of 40%.

Characterization: SEM images were obtained using a field-emission scanning electron microscope (JSM-7500F, JEOL, Japan). Fluorescent optical microscopy images were obtained using a fluorescence microscope (Olympus MX40, Japan). Receding contact angles were measured with a contact angle measurement device (OCA20, DataPhysics, Germany) with latex droplets of 3 μL to be removed dynamically. Each reported receding contact angle was an average of at least five independent measurements. The adhesive force between the particle suspension and substrate was measured using a high-sensitivity microelectromechanical balance system (DataPhysics DCAT 11, Germany). The substrate was immersed into the particle suspension (immersion area: 5 mm × 5 mm) and then lifted vertically at a constant speed (0.001 mm s^{-1}). The surface tension of ink was also measured through DataPhysics DCAT 11.

Supporting Information

Supporting Information is available from the Wiley Online Library or from the author.

Acknowledgements

This work was supported by the 973 Program (2013CB933004), the National Natural Science Foundation of China (NSFC, Grant Nos. 51473173, 51173190, and 21121001), and the "Strategic Priority Research Program" of the Chinese Academy of Sciences (Grant No. XDA09020000).

Received: December 24, 2014
Revised: January 23, 2015
Published online: February 16, 2015

[1] J. S. Miller, K. R. Stevens, M. T. Yang, B. M. Baker, D. H. T. Nguyen, D. M. Cohen, E. Toro, A. A. Chen, P. A. Galie, X. Yu, R. Chaturvedi, S. N. Bhatia, C. S. Chen, *Nat. Mater.* **2012**, *11*, 768.
[2] B. Z. Tian, J. Liu, T. Dvir, L. H. Jin, J. H. Tsui, Q. Qing, Z. G. Suo, R. Langer, D. S. Kohane, C. M. Lieber, *Nat. Mater.* **2012**, *11*, 986.
[3] S. Khetan, M. Guvendiren, W. R. Legant, D. M. Cohen, C. S. Chen, J. A. Burdick, *Nat. Mater.* **2013**, *12*, 458.
[4] M. Kaltenbrunner, T. Sekitani, J. Reeder, T. Yokota, K. Kuribara, T. Tokuhara, M. Drack, R. Schwodiauer, I. Graz, S. Bauer-Gogonea, S. Bauer, T. Someya, *Nature* **2013**, *499*, 458.
[5] Y. J. Na, S. W. Lee, W. Choi, S. J. Kim, S. D. Lee, *Adv. Mater.* **2009**, *21*, 537.
[6] J. T. Muth, D. M. Vogt, R. L. Truby, Y. Menguc, D. B. Kolesky, R. J. Wood, J. A. Lewis, *Adv. Mater.* **2014**, *26*, 5924.
[7] P. Nikolaou, A. M. Coffey, L. L. Walkup, B. M. Gust, C. D. LaPierre, E. Koehnemann, M. J. Barlow, M. S. Rosen, B. M. Goodson, E. Y. Chekmenev, *J. Am. Chem. Soc.* **2014**, *136*, 1636.
[8] L. J. Guo, *Adv. Mater.* **2007**, *19*, 495.
[9] R. E. Ducker, G. J. Leggett, *J. Am. Chem. Soc.* **2006**, *128*, 392.
[10] K. Miszta, J. de Graaf, G. Bertoni, D. Dorfs, R. Brescia, S. Marras, L. Ceseracciu, R. Cingolani, R. van Roij, M. Dijkstra, L. Manna, *Nat. Mater.* **2011**, *10*, 872.
[11] R. Schreiber, J. Do, E. M. Roller, T. Zhang, V. J. Schuller, P. C. Nickels, J. Feldmann, T. Liedl, *Nat. Nanotechnol.* **2014**, *9*, 74.
[12] C. A. Ross, K. K. Berggren, J. Y. Cheng, Y. S. Jung, J. B. Chang, *Adv. Mater.* **2014**, *26*, 4386.
[13] G. M. Gratson, M. J. Xu, J. A. Lewis, *Nature* **2004**, *428*, 386.
[14] J. Hu, M. F. Yu, *Science* **2010**, *329*, 313.
[15] T. D. Brown, P. D. Dalton, D. W. Hutmacher, *Adv. Mater.* **2011**, *23*, 5651.
[16] X. L. Wang, X. B. Cai, Q. Q. Guo, T. Y. Zhang, B. Kobe, J. Yang, *Chem. Commun.* **2013**, *49*, 10064.
[17] G. Villar, A. D. Graham, H. Bayley, *Science* **2013**, *340*, 48.
[18] L. Mishchenko, M. Khan, J. Aizenberg, B. D. Hatton, *Adv. Funct. Mater.* **2013**, *23*, 4577.
[19] B. Su, S. Wang, J. Ma, Y. Wu, X. Chen, Y. Song, L. Jiang, *Adv. Mater.* **2012**, *24*, 559.
[20] B. Su, S. Wang, J. Ma, Y. Song, L. Jiang, *Adv. Funct. Mater.* **2011**, *21*, 3297.
[21] T. S. Wong, S. H. Kang, S. K. Y. Tang, E. J. Smythe, B. D. Hatton, A. Grinthal, J. Aizenberg, *Nature* **2011**, *477*, 443.
[22] E. Ueda, P. A. Levkin, *Adv. Mater.* **2013**, *25*, 1234.
[23] J. Park, J. Moon, *Langmuir* **2006**, *22*, 3506.
[24] W. Han, Z. Lin, *Angew. Chem. Int. Ed.* **2012**, *51*, 1534.
[25] M. X. Kuang, J. X. Wang, B. Bao, F. Y. Li, L. B. Wang, L. Jiang, Y. L. Song, *Adv. Opt. Mater.* **2014**, *2*, 34.
[26] J. X. Wang, Y. Q. Wen, X. J. Feng, Y. L. Song, L. Jiang, *Macromol. Rapid Commun.* **2006**, *27*, 188.
[27] H. Y. Ko, J. Park, H. Shin, J. Moon, *Chem. Mater.* **2004**, *16*, 4212.
[28] B. M. Weon, J. H. Je, *Phys. Rev. E* **2010**, *82*, 015305.
[29] P. J. Yunker, T. Still, M. A. Lohr, A. G. Yodh, *Nature* **2011**, *476*, 308.
[30] R. D. Deegan, O. Bakajin, T. F. Dupont, G. Huber, S. R. Nagel, T. A. Witten, *Nature* **1997**, *389*, 827.
[31] Y. Huang, J. M. Zhou, B. Su, L. Shi, J. X. Wang, S. R. Chen, L. B. Wang, J. Zi, Y. L. Song, L. Jiang, *J. Am. Chem. Soc.* **2012**, *134*, 17053.
[32] T. Furuta, M. Sakai, T. Isobe, A. Nakajima, *Langmuir* **2009**, *25*, 11998.
[33] P. G. Degennes, *Rev. Mod. Phys.* **1985**, *57*, 827.
[34] C. Thornton, *J. Phys. D: Appl. Phys.* **1991**, *24*, 1942.
[35] N. D. Denkov, O. D. Velev, P. A. Kralchevsky, I. B. Ivanov, H. Yoshimura, K. Nagayama, *Langmuir* **1992**, *8*, 3183.
[36] M. Y. Han, X. H. Gao, J. Z. Su, S. Nie, *Nat. Biotechnol.* **2001**, *19*, 631.
[37] H. Kim, J. P. Ge, J. Kim, S. Choi, H. Lee, H. Lee, W. Park, Y. Yin, S. Kwon, *Nat. Photonics* **2009**, *3*, 534.
[38] J. P. Ge, Y. D. Yin, *Angew. Chem. Int. Ed.* **2011**, *50*, 1492.